International Journal on Advanced Science Engineering Information Technology

Vol.15 (2025) No. 2
ISSN: 2088-5334

Leveraging A Robotic Arm Platform for Low-Cost Calibration of Inertial Sensors on LAPAN Sounding Rockets

Khaula Nurul Hakim [a*], Yuniarto Wimbo Nugroho [b], Kandi Rahardiyanti [b], Mirza Zulfikar Rahmat [b], Bagus Wicaksono [b]

[a] *The Research Center for Electronics, National Research and Innovation Agency, South Tangerang City, Banten, Indonesia*
[b] *The Research Center for Rocket Technology, National Research and Innovation Agency, Bogor, West Java, Indonesia*
Corresponding author: [*]khau001@brin.go.id

***Abstract*—The technology has enabled the widespread use of multisensory integration such as inertia sensors for the localization of inertia and navigation systems. The accuracy of the measurement is a key factor that must be maintained and is influenced by default sensor errors (scale factor, misalignment and bias). Thus, this study focuses on proper calibration (complementary filter) to minimize the invalidation of sensor data. The proposed calibration system applies correction of the accelerometer and gyroscope bias data to the x, y, and z axes. Application to the motion of each axis was carried out on the data surface of a robot arm by adjusting the expected axis in the positive or negative areas. For bias correction or compensated distortion of the accelerometer, low pass filter to eliminate deviation and noise was applied into Arduino software. While, for bias correction or compensated distortion of the gyroscope used high-pass filter via software to allow short-term signals and prevents long-term fluctuations. Consequently, this proposed Inertia Measurement Unit (IMU) calibration system demonstrates a high accuracy at estimating the offset of an object. As a result, the accelerometer data of uncalibration and calibration are [14,29 17,38 –22,57] and [1,56 -4,26 -1,91], respectively, while gyroscope resulted uncalibration data [-4,78 0,72 -3,39] and calibration data are [-0.15 0,64 -0,39]. The results highlight the importance of the calibration process for precise sensor data.**

***Keywords*— Inertia measurement unit; calibration; robotic arm; complementary filter; fixed bias.**

Manuscript received 5 Nov. 2024; revised 19 Jan. 2025; accepted 9 Apr. 2025. Date of publication 30 Apr. 2025.

I. INTRODUCTION

The rocket developed by the Rocket Technology Center at ORPA BRIN includes several systems such as propulsion, propellant, avionics and flight control systems for both military and scientific applications [1]. To measure an object's orientation and position in space, inertial sensors, also known as Inertial Measurement Units (IMUs), are commonly used. These sensors track an object's rotation and provide data on gravitational force, angular velocity, and orientation by utilizing accelerometers, gyroscopes, and magnetometers [2], [3]. IMUs serve as the core component in inertial navigation systems (INS) for unmanned aerial vehicles (UAVs) and inertial guidance systems used in missiles, as well as on ships, submarines, and space shuttles [4], [5], [6]. Having a small size and being lightweight makes IMUs well suited to the purpose. Consequently, the inertial systems were created for sophisticated robotic applications, such as estimating wheel slip and localizing a steering mobile robot to ascertain the location and orientation of unmanned underwater vehicles (UUVs) [7], [8], [9], [10].

In these implementations, to give a precise value and provide a valid alternative to specific expensive tools, such as the optical camera tracking system, a high accuracy estimation of the object orientation is required [11], [12]. Three mutually orthogonal sensitive axes are required to measure in three dimensions. The MARG (magnetic, angular rate, and gravity) system, also known as an AHRS (attitude and heading reference systems), is capable of precisely determining orientation in relation to the earth's magnetic field and gravitational direction [13], [14]. An AHRS with onboard computational ability to generate object attitude information (yaw, pitch, and roll) from raw sensor data is thus incorporated into the IMU [15], [16], [17].

In order to enable accurate measurements right away, many industrial IMUs are factory-calibrated, with the calibration parameters for each sensor being saved in firmware or nonvolatile memory. However, this calibration process

increases sensor costs due to the time-consuming comparison with reference standards and the need for specialized equipment. In contrast, low-cost IMUs typically have poor calibration, resulting in measurements with notable errors. Their reduced performance is particularly evident during fast or dynamic motions, where linear acceleration and rotational axes shift rapidly. Some calibration techniques use the orientation of a hand-held accelerometer to obtain minimum and maximum values, then multiply the two values to produce an offset and scale the distance from maximum to minimum to 2g [18]. In a given duration, gyro scaling is calculated by rotating the IMU at a certain angle and is separated by the integrated gyro signal. An alternative calibration method can be proposed for field use by utilizing a specialized Kalman filter that leverages zero-velocity measurement updates [19]. This method successfully lowers errors during motion, increasing the accuracy of hand-performed calibration. Comprehensive simulations and actual tests are used to evaluate and validate the effectiveness of this calibrating technique, demonstrating its reliability and effectiveness in practical scenarios [20].

Cao et al. [21] proposed an automated calibration method that evaluates the optimization errors of three key parameters: each sensor's scaling factors, biases, and misaligned angles. The method involves rotating the sensors around all axes and holding them in twelve distinct positions. However, the calibration method did not fully account for the similarity between the angles of the accelerometer and magnetometer matrices, which could affect accuracy. Additionally, the gyroscope relied on data from another calibrated sensor for its calibration, but the specific details of this process were not provided [22] . Over time, small inaccuracies in scaling, bias, and angle alignment can compound, leading to incorrect readings. This impacts the reliability of sensor data, reduces the precision of motion tracking, and necessitates more frequent recalibration to maintain accuracy.

To create a robust IMU, a combination of accelerometers, gyroscopes, and magnetometers are incorporated to determine the target of an optimal sensor fusion algorithm that accurately calculates orientation. This study is proposed to acquire a fairly straightforward yet precise method for calibrating inertial sensor of commercial grade. The suggested calibration is tailored for a sensor model with six parameters (offset and gain for each axis), making it highly suitable for consumer-grade IMUs. However, this approach also has the potential to calibrate more advanced sensor models.

II. Materials And Method

The study discusses the use of a combination of low-pass and high-pass filters in determining the orientation of flight objects. The low-pass filter is used by accelerometer to eliminate deviation and noise errors, while the high-pass filter (gyroscope) allows short-term signals and prevents long-term fluctuations. The complementary filter, used for sensors with complementary frequency characteristics, is used to accurately determine the orientation of the flight object. The proposed calibration system consists of three segments which are deterministic error, experimental setup, and data collection. In simple terms, the data taken is IMU data from the accelerometer and gyroscope sensors placed on the flat surface of the robotic arm. In the calibration of the accelerometer sensor, the sensor is at an angle of 0º, ±90º, ±180 º in a stationary condition while the gyroscope sensor is done by moving the sensor inside the robot arm at an angle of 0º to 90º, and 90º to 180º.

A. Deterministic and Measurement Error Model

Fixed biases, scale factors, and misalignment errors are the three primary categories of data error in IMU measurements. Regardless of the forces or levels applied to the sensor, measurement inaccuracies known as bias are present in both the accelerometer and the gyroscope. Bias can be classified into unstable, stable, and fixed. In IMU measurements, the variable biases, also referred to as an offset, are deterministic biases that are modifiable. Biases in instability can be changed in a time function as a random process, and stability can change randomly from run to run [23], [24]. Errors in the scale factor, as shown in Figure 1, explain how the sensor's output matches the force input or rate. This method can model the difference between a linear measurement slope generated by an IMU and an ideal one-way input-output slope. A linear response is also commonly used to display an IMU to make measurement computations easier. Non-linearities, on the other hand, could introduce more flaws into a study.

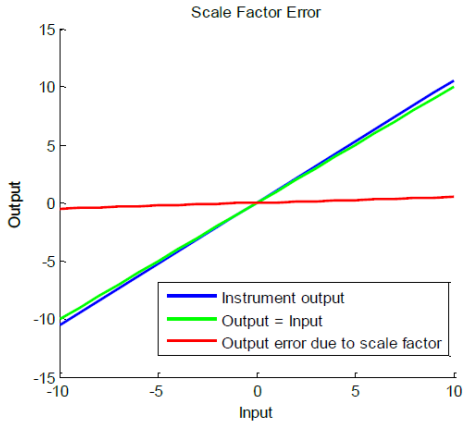

Fig. 1 Scale Factor Error

Misalignment errors arise from improper construction or alignment of the three sensor axes in an accelerometer and gyroscope [25]. Figure 2 illustrates how the forces on the other two axes cause erroneous readings on the sense-axis when the sense-axis is not exactly aligned with the body-axis to be calculated, scale factor and misalignment errors are integrated into a single matrix for an accelerometer or gyroscope (1).

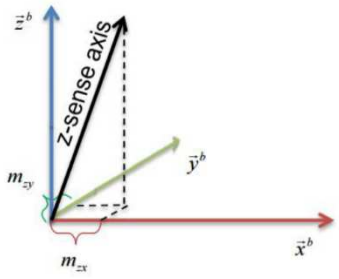

Fig. 2 Misalignment Error

$$Ma = \begin{bmatrix} Sa,x & Ma,xy & Ma,xz \\ Ma,yx & Sa,y & Ma,yz \\ Ma,zx & Ma,zy & Sa,z \end{bmatrix}$$
$$Mg = \begin{bmatrix} Sg,x & Mg,xy & Mg,xz \\ Mg,yx & Sg,y & Mg,yz \\ Mg,zx & Mg,zy & Sg,z \end{bmatrix} \quad (1)$$

Gulf coast data [26] describes a calibration technique that uses tumble to improve the accelerometer detector's accuracy. Gravity is used as an acceleration of the relation in this measurement technique. In order to fine-tune the sensor's linear relationship, a scaling factor and offset factor are determined by placing each axis in and out of the gravity vector, yielding reference points of +1g, -1g, and 0g.

Typically, the gyroscope and accelerometer's 3-D sensitive axes should be in the same orthogonal frame. These frames will be called the *a*-frame (*xa, ya, za*) and the g-frame (*xg, yg, zg*), respectively, and are defined by sensitive axes. Regretfully, the gyroscope and accelerometer frames are not coincident and nonorthogonal. The other two axes in the same cluster will feel some of the acceleration given to one of the axes because of the accelerometer cluster's nonorthogonality. A key component of the conceptual framework that forms the basis of the system is the platform frame, also called the *p*-frame (*xp, yp, zp*). This frame will serve as the basis for accelerometer and gyroscope data. Figure 3 illustrates how the accelerometer's sensing axis, *xa*, and the *xp*-axis are initially intented to line up. As a result, accelerations along the plaform frame's *yp*- and *zp*-axes cannot affect *xa* since *xp* is by definition exactly 90◦ to these axes. Consequently, $\alpha x\, y$ and $\alpha x\, z$ are zero, and $\alpha i\, j$ is the part of the *jth* frame acceleration that the accelerometer's *ith* axis detects. A similar definition applies to the other axes, *yp* and *zp*. After defining the platform frame, each gyro's two misalignment terms ($\beta i\, j$) need to be taken into account. Consequently, six gyro misalignment terms exist [27]. The fundamental model for the forces (measured accelerometer outputs) represented by $f_s = [f_{x,s} \quad f_{y,s} \quad f_{z,s}]^T$ proposed by Reference[28] is:

$$f_s = S_f f^\alpha + b_f + v_f \quad (2)$$

where $f^\alpha = [f_x^\alpha \quad f_y^\alpha \quad f_z^\alpha]^T$ is the calibrated force vector, $b_f = [\, b_x \quad b_y \quad b_{z,}]^T$is the offset or biases vector and

$$S_f = \begin{bmatrix} 1+s_x & 0 & 0 \\ 0 & 1+s_y & 0 \\ 0 & 0 & 1+s_z \end{bmatrix} \quad (3)$$

is the diagonal matrix of the scale factor, and v_f is the random noise. The three accelerometer sensitivity axes, represented by α , are the subject of the calibrated forces f^α. These axes should ideally be orthogonal, although this is probably not the case because of inaccurate manufacture. In order to accommodate this non-orthogonality of the sensor sensitivity axis, another study by [29] expanded their model by adding the following formula:

$$f^p = T_a^p f^\alpha \text{ , with } T_\alpha^p = \begin{bmatrix} 1 & -\alpha_{yz} & \alpha_{zy} \\ \alpha_{xz} & 1 & -\alpha_{zx} \\ -\alpha_{xy} & \alpha_{yx} & 1 \end{bmatrix} \quad (4)$$

which uses six parameters to convert the sensitivity axes to the orthogonal body or frame (represented by *p*). In this case, these parameters can be understood as tiny angles, where αij represents the *i*-th axis rotation around the *j*-th body axis (see Figure 3). Equation (4) turns into a skew-symmetric matrix, which is equivalent to the well-knows small angle approximation rotation matrix, if both rotations about one axis are equal, for instantce, $\alpha_{xz} = \alpha_{yz}$ for all rotation axes. Equation (4) reduces to (see Figure 3) when the body frame is defined so that *x*-axes coincide and y^b-axis is the plane that is covered by x^a and y^a.

$$f^p = T_\alpha^p f^\alpha \text{ , with } T_\alpha^p = \begin{bmatrix} 1 & -\alpha_{yz} & \alpha_{zy} \\ 0 & 1 & -\alpha_{zx} \\ 0 & 0 & 1 \end{bmatrix} \text{ and}$$
$$T_\alpha^{p-1} = T_\alpha^p = \begin{bmatrix} 1 & \alpha_{yz} & \alpha_{zx}\alpha_{zy} - \alpha_{yz} \\ 0 & 1 & \alpha_{zx} \\ 0 & 0 & 1 \end{bmatrix} \quad (5)$$

By expanding (2) and (5) which includes three more non-orthogonality parameters $\alpha_f = [\, \alpha_{zx} \quad \alpha_{zy} \quad \alpha_{yz}]^T$, a nine-parameter model is produced.

$$f_s = S_f T_\alpha^p f^p + b_f + v_f \quad (6)$$

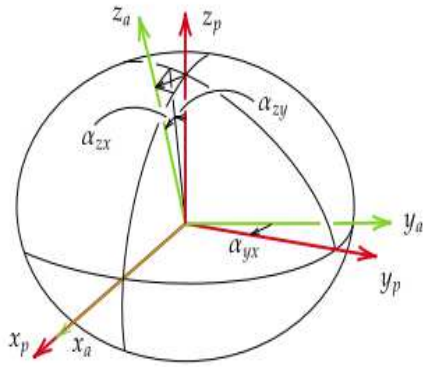

Fig. 3 Misalignment of accelerometer frame and platform frame

whereas the gyro-sensitive framework and the angle of motion vectors found in the structure are displayed by the Equation:

$$\omega_s = [\omega_{x,s} \;\; \omega_{y,s} \;\; \omega_{z,s}]^T \text{and } \omega_p = [\omega_{x,p} \;\; \omega_{y,p} \;\; \omega_{z,p}]^T \quad (7)$$

The following misalignment phrases can be used to relate the relationship between the platform frame and each inertial sensor's sensitive axis [30]:

$$\omega_{ip}^p = T_g^p \omega_{ig}^g \text{ with } T_g^p = \begin{bmatrix} 1 & -\gamma_{yz} & \gamma_{zy} \\ \gamma_{xz} & 1 & -\gamma_{zx} \\ -\gamma_{xy} & \gamma_{yx} & 1 \end{bmatrix} \quad (8)$$

B. Experimental Setup

The initial phase of this study uses an IMU sensor to capture acceleration, gyration, and magnetic field data. The MPU-9250 is used, which combined MPU6050, an accelerometer, gyroscope, and magnetometer in a single chip, and AK896327, a 3-axis digital compass, which prevents cross-axis misalignment issues [31], [32]. The sensor is connected to a microcontroller unit (MCU Arduino Uno R3) via an I2C channel at up 400KHz [33], as shown in Figure 4. The I2C pin

on the sensor transmits input data, which is then sent to a computer through USB communication. Subsequently, the data comprising feature extraction, feature scaling, fixed bias adjustments, and calibration data generation is processed.

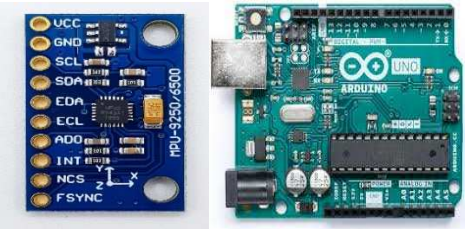

Fig. 4 Sensor IMU (9250) with Arduino Uno R3

The IMU calibration data is applied to a robotic arm that is aligned on a flat surface to obtain precise measurements for estimating the object's orientation, as shown in Figure 5. The Veyron servo driver is a 24-channel development board for robots, spiders, and robotic arms. It features real-time, timer, and constant speed control modes. The driver is capable of high reliability, performance, and low-power STM32F103 microcontrollers, with servo control range from 0º to 180°. The study uses Arduino IDE and a Veyron servo controller for programming and debugging IMU sensor. Arduino IDE is used for IMU sensor programming and debugging, while DFServo controls servos. DFServo allows users to complete multiple movements simultaneously.

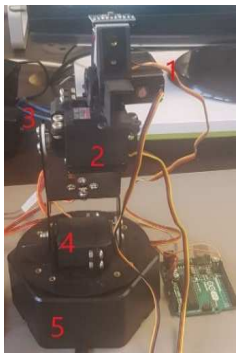

Fig. 5 Robotic arm on a flat surface

C. Data Collection

In the sensor measurements, offset is the average waveform value. It indicates that there is no offset, and the value is equal to zero. All MEMS-based sensors integrated with accelerometers and gyroscopes still provide values that are close to zero. Every gadget has a reason for maintaining its offset, which is typically used to determine orientation. Therefore, each device has a unique approach for calculating and correcting offsets. Fig. 6 illustrates the flow of this calibration data collection.

The offset is rather substantial because the gravitational pull always impacts the accelerometer. Because it is easy to reduce the gravitational offset, the MPU9250 is installed with the z-axis facing upward. There is no movement where this sensor is installed. However, the offset is still present in the raw output as an average in the output waveform. To get the exact data, even when moving, this offset must thus always be subtracted from the raw accelerometer signal. The accelerometer data is used to estimate gravity to calculate orientation. Therefore, it is still necessary to reduce the offset without using the gravity component [29].

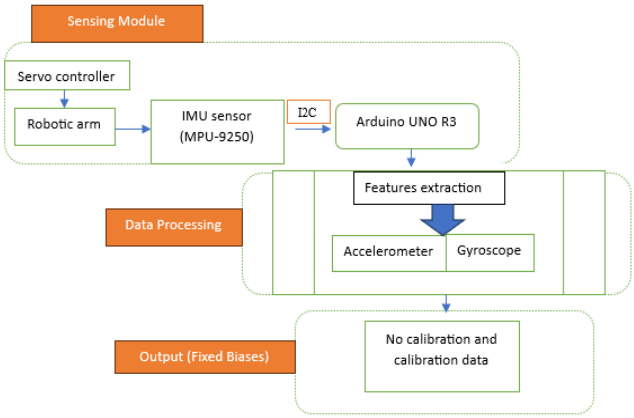

Fig. 6 Data Collection

Since the unit is fixed in a position that corrects the gyroscope misalignment, it would record zero angular velocity while still in static mode. If there is a non-zero fraction of the electronic converter in the raw data, it is the gyroscope offset. To update these offsets, the non-zero values from the original data should be constantly subtracted. After that, the waveform is aligned with the time axis, and every interpretation results in movements.

III. Results and Discussion

The accelerometer and gyroscope are calibrated using data supplied by the robotic arm's output rate. Three preset bias values (offset) are calculated to determine the calibration terms. A single six-direction test can be used to determine the sensor's calibration variables [34]. In a model test, the accelerometer's sense-axis was aligned with gravity and 210 second readings are taken. The data pertaining to +z-axis and -z-axis are shown in Figures 7 (a), (b), (c), and (d). The accelerometer data has a magnitude of g, where 1g is equivalent to 9.81 m/s².

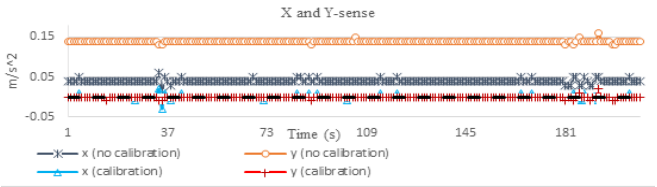

Fig. 7 (a) X and Y-sense at +z-axis (*g*)

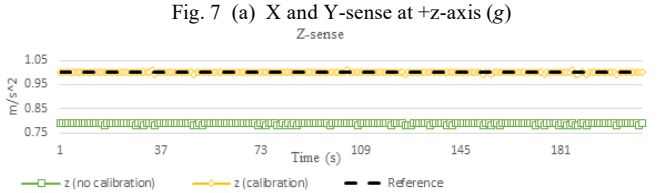

Fig. 7 (b) Z-sense at +z-axis test (*g*)

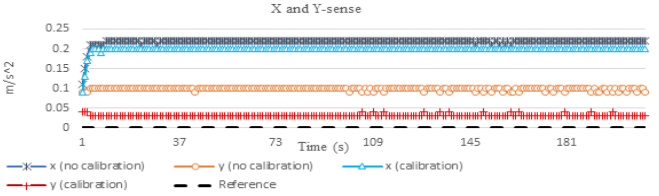

Fig. 7 (c) X and Y-sense at -Z-axis (*g*)

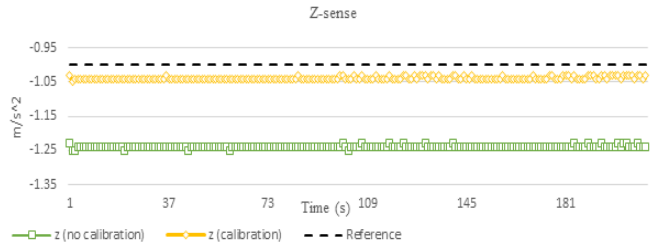

Fig. 7 (d) Z-sense at -z-axis (*g*)

Figures 8 (a), (b), (c), and (d) show the results of the x-axis test for accelerometer measurements.

Fig. 8 (a) X-sense at +X-axis (*g*)

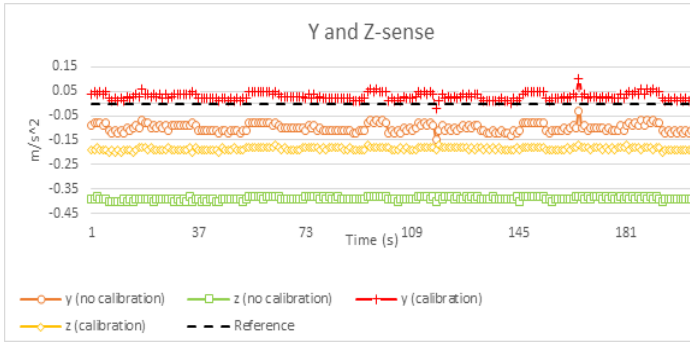

Fig. 8 (b) Y and Z-sense at +X-axis (*g*)

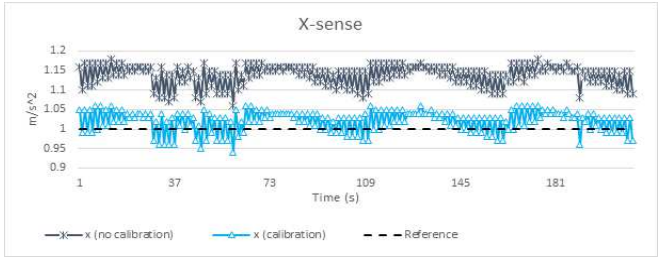

Fig. 8 (c) X-sense at -X-axis (*g*)

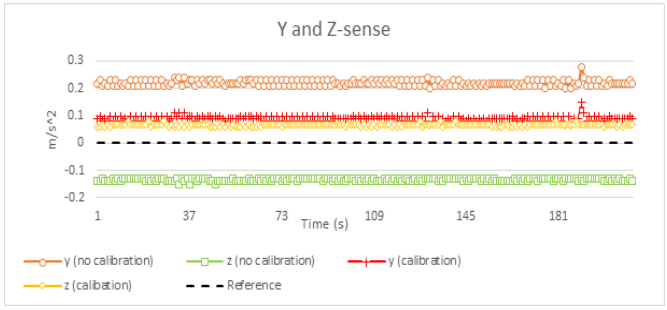

Fig. 8 (d) Y and Z-sense at -X-axis (*g*)

Figures 9 (a), (b), (c), and (d) show the results of the y-axis test for accelerometer measurements.

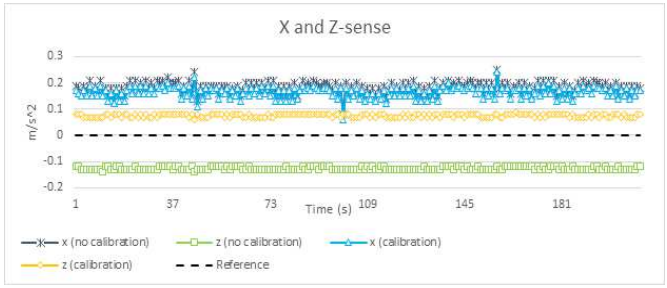

Fig. 9 (a) X and Z-sense at +Y-axis (*g*)

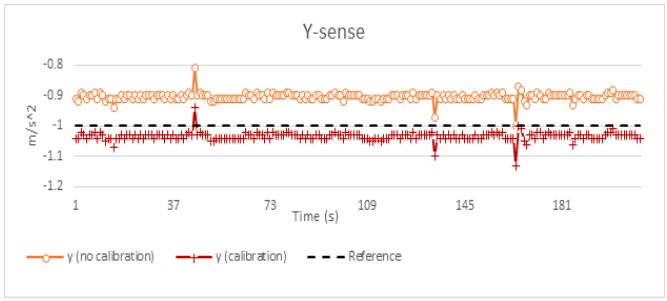

Fig. 9 (b) Y-sense at +Y-axis (*g*)

Fig. 9 (c) X and Z-sense at -Y-axis (*g*)

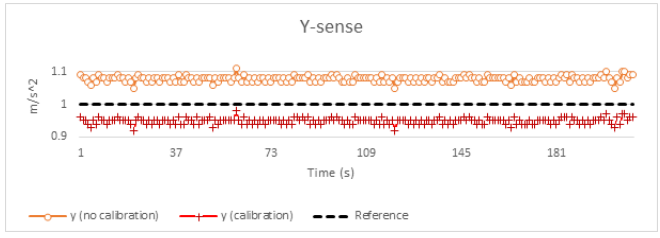

Fig. 9 (d) Y-sense at -Y-axis (*g*)

The acceleration measurement involves rotation through the x, y, and z axes (positive and negative). Each orientation should yield acceleration values on the active axis, while the values on the other axes should be close to zero. As a result of Figures (7), (8), and (9), a comparison is visible between the measured acceleration values and the ideal values of ±9.81 m/s². Scaling adjustments result in accurate values, as the ratio between the sensor output and the actual value does not exceed 1. The residual values from accelerometer measurements (bias) for each axis need to be corrected.

The fixed bias of the accelerometer can be measured using formula (9). The (+) data characterized the positively aligned axis, while the (-) data described the negatively aligned axis. This computation uses the mean value of the measurements on the aligned axes. Table I shows the fixed bias calculator from no calibration data, and Table II displays the fixed bias data from the 6-direction test, respectively.

$$b_{a,FB} = \begin{bmatrix} f_{ib,x}^{b,+} + f_{ib,x}^{b,-} \\ f_{ib,y}^{b,+} + f_{ib,y}^{b,-} \\ f_{ib,z}^{b,+} + f_{ib,z}^{b,-} \end{bmatrix} 1/2 \quad (9)$$

TABLE I
AVERAGED ACCELEROMETER UN-CALIBRATION DATA (ALIGNED WITH GRAVITY)

Sense	X(+)	Y(+)	Z(+)	X(-)	Y(-)	Z(-)
X	1.1392	0.2249	0.0404	-0.8533	0.1825	0.2183
Y	0.2205	1.0777	0.1398	-0.0991	-0.9039	0.0985
Z	-0.1344	-0.0581	0.7882	-0.3876	-0.1265	-1.2396

$$b_{a,FB}\ (No\ calibration) = \begin{bmatrix} 14.29 \\ 17.38 \\ -22.57 \end{bmatrix} mg$$

TABLE II
AVERAGED ACCELEROMETER CALIBRATION DATA (ALIGNED WITH POSITIVE GRAVITY)

Sense	X(+)	Y(+)	Z(+)	X(-)	Y(-)	Z(-)
X	1.1393	0.2250	0.0404	-0.8533	0.1826	0.2183
Y	0.2205	1.0778	0.1396	-0.0991	-0.9039	0.0985
Z	-0.1344	-0.0581	0.7882	-0.3877	-0.1265	-1.2396

$$b_{a,FB}\ (Calibration) = \begin{bmatrix} 1.56 \\ -4.26 \\ -1.91 \end{bmatrix} mg$$

The fixed bias data obtained from uncalibrated data as shown in Table I is [14.29 17.38 -22.57] mg. These values indicate significant bias on all three axes, especially the Z-axis −22.57 mg. High bias can cause substantial inaccuracies in acceleration readings. After calibration as shown in Table II, the bias values are significantly reduced on all axes. The calibrated values are close to zero, indicating improved accuracy. X-axis: bias reduced from 14.29 mg to 1.56 mg, y-axis: bias reduced from 17.38 mg to −4.26 mg, and z-axis: bias reduced from −22.57 mg to −1.91 mg.

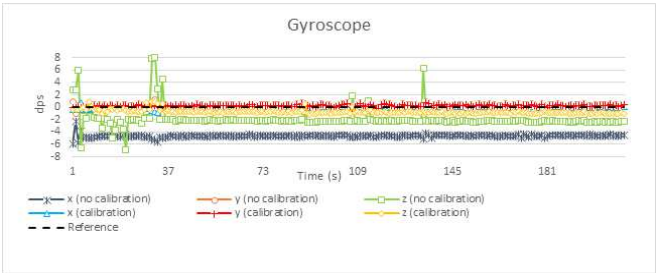

Fig. 10 (a) +Z-axis Test (dps)

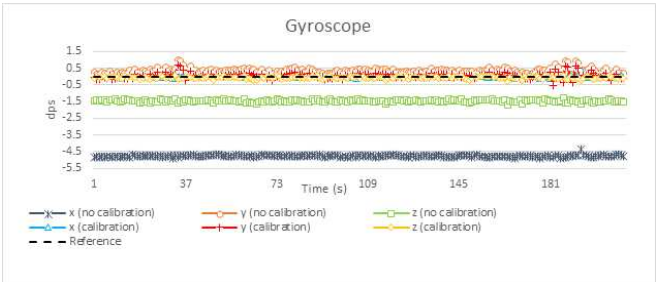

Fig. 10 (b) -Z-axis Test (dps)

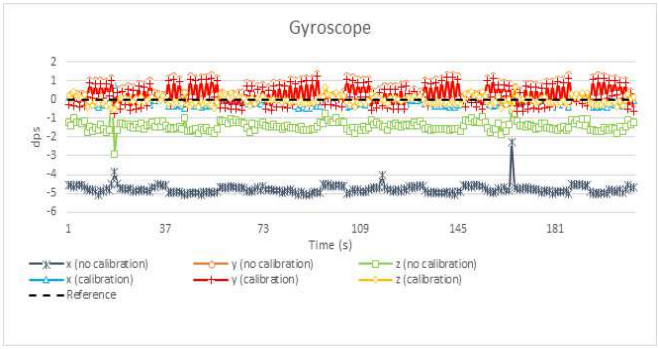

Fig. 10 (c) +X-axis Test (dps)

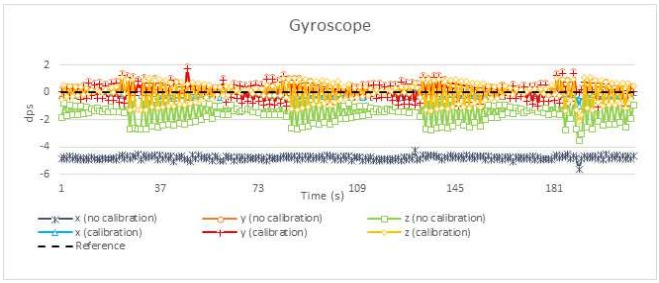

Fig. 10 (d) -X-axis Test (dps)

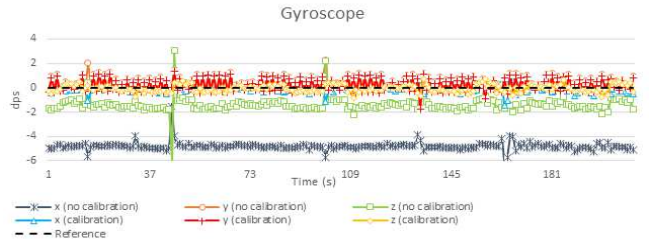

Fig. 10 (e) +Y-axis Test (dps)

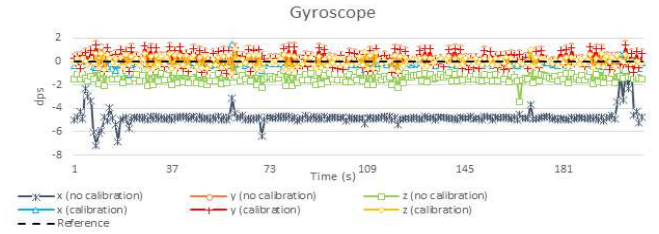

Fig. 10 (f) -Y-axis Test (dps)

The 6-direction test model is a straightforward yet effective approach for calibrating a gyroscope's fixed bias (offset). Six specific orientations correspond to the positive and negative directions of the x, y, and z axes. This method can identify and correct the fixed bias in various orientations and directions, ensuring that all potential bias errors on each axis are detected and corrected. The gyroscope output is displayed in Figures 10 (a), (b), (c), (d), (e) and (f).

The raw data obtained from testing consists of the raw readings from the gyroscope sensor for each previously determined orientation. This data will indicate the angular velocity along each axis (X, Y, Z) for each sensor orientation (+X, -X, +Y, -Y, +Z, -Z). The gyroscope readings are in the form of angular velocity values (degrees per second) along the x, y, and z axes. This data is collected while the sensor is stationary, so that every change in the values should be caused by the sensor's fixed bias, not due to actual rotation. This bias represents the difference between the expected sensor

readings (which should be 0 if the sensor is not rotating) and the actual values measured by the sensor.

The fixed bias of the gyroscope can be measured using formula (10). The (+) data characterized the positively aligned axis, while the (-) data described the negatively aligned axis. This computation uses the mean value of the measurements on the aligned axes. Tables III (uncalibration) and IV (calibration) below show the gyroscope data from the 6-direction test.

$$b_{g,FB} = \begin{bmatrix} \omega_{ib,x}^{b,+} + \omega_{ib,x}^{b,-} \\ \omega_{ib,y}^{b,+} + \omega_{ib,y}^{b,-} \\ \omega_{ib,z}^{b,+} + \omega_{ib,z}^{b,-} \end{bmatrix} 1/2 \qquad (10)$$

TABLE III
AVERAGED GYROSCOPE UN-CALIBRATION DATA (ALIGNED WITH GRAVITY)

Sense	X(+)	Y(+)	Z(+)	X(-)	Y(-)	Z(-)
X	-4.7844	0.2249	-4.7728	-4.7779	-4.8179	-4.6306
Y	0.2636	1.0778	0.3377	0.3618	0.3626	0.3715
Z	-1.3873	-0.0581	-1.4723	-1.4163	-1.4182	-1.9170

$$b_{g,FB}\ (No\ calibration) = \begin{bmatrix} -4.78 \\ 0.72 \\ -3.39 \end{bmatrix} dps$$

TABLE IV
AVERAGED GYROSCOPE CALIBRATION DATA (ALIGNED WITH GRAVITY)

Sense	X(+)	Y(+)	Z(+)	X(-)	Y(-)	Z(-)
X	-0.1515	0.2249	0.0051	-0.1573	-0.2002	-0.0015
Y	0.1262	1.0778	0.0477	0.2249	0.2081	0.2311
Z	0.0018	-0.0581	-0.068	-0.0375	-0.0637	-0.7095

$$b_{g,FB}\ (Calibration) = \begin{bmatrix} -0.15 \\ 0.64 \\ -0.39 \end{bmatrix} dps$$

The fixed bias from gyroscope obtained from uncalibrated data, as shown in Table III is [-4.78 0.72 -3.39] dps, while fixed bias from calibrated data, as shown in Table IV is [-0.15 0.64 -0.39]. On the x-axis, there was a significant reduction in bias from -4.78 dps to -0.15 dps, y-axis: the reduction in bias was smaller, from 0.72 dps to 0.64 dps, and on thez-axis, calibration reduced the bias from -3.39 dps to -0.39 dps.

IV. CONCLUSION

The IMU was calibrated with the fixed biases of each sensor accelerometer and gyroscope using the robotic arm. The study implemented the use of a combination of low-pass and high-pass filters in determining the orientation of inertial sensor. A calculation was performed to measure the bias parameters of raw data so that it could be corrected properly. The low-pass filter eliminates deviation and noise errors, while the high-pass filter allows short-term signals and prevents long-term fluctuations. In a result, the accelerometer data of no calibration is [14,29 17,38 –22,57] mg. After calibration, the residual bias value [1.56 −4.26 −1.91] mg is within acceptable limits for most applications, reducing errors in measurements. Calibration significantly reduces the fixed bias of the accelerometer on all three axes. While the gyroscope resulted in no calibration data [-4,78 0,72 -3,39], and calibration data are [-0.15 0,64 -0,39]. The comparison between the uncalibrated and calibrated data shows that the calibration process effectively reduces the fixed bias on the gyroscope. The smaller bias values after calibration on the x and z axes demonstrate that calibration successfully corrected the sensor errors present in the uncalibrated data. The calibration improved the accelerometer and gyroscope readings, making measurements more accurate.

Although the calibration process significantly reduces fixed bias and improves the accuracy of accelerometer and gyroscope measurements, further research is needed to refine and enhance the calibration methodology. Future research could focus on automated calibration techniques, implementing machine learning or AI-based methods to optimize calibration, reduce manual intervention, and improve efficiency.

ACKNOWLEDGMENT

This research was supported by the Research Center of Rocket Technology (PRTR) from the Aeronautics and Space Research Organization (ORPA) and the Research Center for Electronics (PRE) from the Electronic and Informatics Research Organization (OREI). The authors are also immensely grateful to the National Research and Innovation Agency of Indonesian (BRIN) for their support in this research activity.

REFERENCES

[1] D. Deswandri *et al.*, "Risk Assessment of Solid Propellant Rocket Motor using a Combination of HAZOP and FMEA Methods," *Journal of Advanced Research in Fluid Mechanics and Thermal Sciences*, vol. 110, pp. 63–78, Oct. 2023, doi: 10.37934/arfmts.110.1.6378.

[2] Kurdianto *et al.*, *Design and Testing of Data Communication System Integration on RX-450.03 Sounding Rocket*. 2023. doi:10.1109/agers61027.2023.10490808.

[3] P. Sonchan, N. Ratchatanantakit, N. O-Larnnithipong, M. Adjouadi, and A. Barreto, "Robust Orientation Estimation from MEMS Magnetic, Angular Rate, and Gravity (MARG) Modules for Human–Computer Interaction," *Micromachines (Basel)*, vol. 15, no. 4, 2024, doi: 10.3390/mi15040553.

[4] C. Shi, X. Chen, and J. Wang, "An improved multi-source information fusion method for IMU compensation of missile," *EURASIP J Adv Signal Process*, vol. 2023, Jul. 2023, doi: 10.1186/s13634-023-01047-6.

[5] Q. Wang *et al.*, "Recent Advances in Pedestrian Inertial Navigation Based on Smartphone: A Review," *IEEE Sens J*, vol. PP, p. 1, Dec. 2022, doi: 10.1109/jsen.2022.3213836.

[6] A. Tavares Júnior and N. Oliveira, "A Novel Approach for Kalman Filter Tuning for Direct and Indirect Inertial Navigation System/Global Navigation Satellite System Integration," *Sensors*, vol. 24, p. 7331, Nov. 2024, doi: 10.3390/s24227331.

[7] H. Xing *et al.*, "A Multi-Sensor Fusion Self-Localization System of a Miniature Underwater Robot in Structured and GPS-Denied Environments," *IEEE Sens J*, vol. PP, p. 1, Oct. 2021, doi:10.1109/jsen.2021.3120663.

[8] L. Zhang, X. Cao, M. Su, and Y. Sui, "Collaborative Integrated Navigation for Unmanned Aerial Vehicle Swarms Under Multiple Uncertainties," *Sensors*, vol. 25, p. 617, Jan. 2025, doi:10.3390/s25030617.

[9] S. Liang, X. Dong, T. Guo, F. Zhao, and Y. Zhang, "Peripheral-Free Calibration Method for Redundant IMUs Based on Array-Based Consumer-Grade MEMS Information Fusion," *Micromachines (Basel)*, vol. 13, no. 8, 2022, doi: 10.3390/mi13081214.

[10] J. Liu, Z. Deng, and M. Fu, "A Model-Free Calibration Method of Inertial Navigation System and Doppler Sensors," *IEEE Sens J*, vol. PP, p. 1, Aug. 2020, doi: 10.1109/jsen.2020.3015845.

[11] A. Miller, B. Miller, and G. Miller, "Navigation of Underwater Drones and Integration of Acoustic Sensing with Onboard Inertial Navigation System," *Drones*, vol. 5, p. 83, Aug. 2021, doi:10.3390/drones5030083.

[12] P. Franček, K. Jambrošić, M. Horvat, and V. Planinec, "The Performance of Inertial Measurement Unit Sensors on Various Hardware Platforms for Binaural Head-Tracking Applications," *Sensors*, vol. 23, no. 2, 2023, doi: 10.3390/s23020872.

[13] N. Navidi and R. Landry, "A New Perspective on Low-Cost MEMS-Based AHRS Determination," *Sensors*, vol. 21, no. 4, 2021, doi:10.3390/s21041383.

[14] W. Ding, W. Sun, H. Yan, Y. Jiang, and Y. Gao, "Attitude estimation in challenging environments by integrating low-cost dual-antenna GNSS and MEMS MARG sensor," *GPS Solutions*, vol. 29, Jan. 2025, doi: 10.1007/s10291-024-01805-5.

[15] Y. Lu, Z. Li, J. Xiong, and K. Lv, "Adaptive UAV Navigation Method Based on AHRS," *Sensors*, vol. 24, p. 2518, Apr. 2024, doi:10.3390/s24082518.

[16] G. Kopecki and M. Banicki, "A proposal of AHRS yaw angle correction with the use of roll angle," *Aircraft Engineering and Aerospace Technology*, vol. 95, Apr. 2023, doi: 10.1108/aeat-10-2022-0274.

[17] S. O. H. Madgwick, S. Wilson, R. Turk, J. Burridge, C. Kapatos, and R. Vaidyanathan, "An Extended Complementary Filter for Full-Body MARG Orientation Estimation," *IEEE/ASME Transactions on Mechatronics*, vol. 25, no. 4, pp. 2054–2064, 2020, doi:10.1109/tmech.2020.2992296.

[18] H. Al-Jlailaty and M. M. Mansour, "Efficient Attitude Estimators: A Tutorial and Survey," *J Signal Process Syst*, vol. 94, no. 11, pp. 1309–1343, 2022, doi: 10.1007/s11265-020-01620-4.

[19] X. Wang, J. Li, G. Xu, and X. Wang, "A Novel Zero-Velocity Interval Detection Algorithm for a Pedestrian Navigation System with Foot-Mounted Inertial Sensors," *Sensors*, vol. 24, no. 3, 2024, doi:10.3390/s24030838.

[20] Y.-B. Seo *et al.*, "Analysis of Gyro Bias Depending on the Position of Inertial Measurement Unit in Rotational Inertial Navigation Systems," *Sensors*, vol. 22, p. 8355, Oct. 2022, doi: 10.3390/s22218355.

[21] C. Cao, C. Wang, S. Zhao, T. Tan, L. Zhao, and F. Zhang, "Underwater Gyros Denoising Net (UGDN): A Learning-Based Gyros Denoising Method for Underwater Navigation," *J Mar Sci Eng*, vol. 12, no. 10, 2024, doi: 10.3390/jmse12101874.

[22] H. Jlailaty, A. Çelik, M. Mansour, and A. Eltawil, "IMU Hand-Calibration for Low-Cost MEMS Inertial Sensors," *IEEE Trans Instrum Meas*, vol. PP, p. 1, Jan. 2023, doi:10.1109/tim.2023.3301860.

[23] Y. Bolotin and V. Savin, "Turntable IMU Calibration Algorithm Based on the Fourier Transform Technique," *Sensors*, vol. 23, no. 2, 2023, doi: 10.3390/s23021045.

[24] J. Ban, G. Chen, Y. Meng, and J. Shu, "Calibration method for misalignment angles of a fiber optic gyroscope in single-axis rotational inertial navigation systems," *Opt Express*, vol. 30, p. 6487, Feb. 2022, doi: 10.1364/OE.449629.

[25] J. Ye, L. Wang, H. Han, Z. Zhan, and L. Yan, "Alignment scheme optimization when gyro accuracy inconsistency for inertial navigation system," *Measurement*, vol. 216, p. 112893, 2023, doi:10.1016/j.measurement.2023.112893.

[26] B. Constantin, D. Iozsa, and C. Stan, "Experimental research on pedestrian lower leg impact," *IOP Conf Ser Mater Sci Eng*, vol. 252, p. 012006, Oct. 2017, doi: 10.1088/1757-899X/252/1/012006.

[27] P. Wang, B. Lu, P. Yang, and F. Chen, "Systematic calibration method based on acceleration and angular rate measurements for fiber-optic gyro SINS," *Review of Scientific Instruments*, vol. 92, no. 1, p. 015001, Jan. 2021, doi: 10.1063/5.0023674.

[28] C. Gao, G. Wei, L. Wang, Q. Wang, and Z. Liao, "A Systematic Calibration Modeling Method for Redundant INS with Multi-Sensors Non-Orthogonal Configuration," *Micromachines (Basel)*, vol. 13, no. 10, 2022, doi: 10.3390/mi13101684.

[29] J. C. Lötters, J. Schipper, P. H. Veltink, W. Olthuis, and P. Bergveld, "Procedure for in-use calibration of triaxial accelerometers in medical applications," *Sens Actuators A Phys*, vol. 68, no. 1, pp. 221–228, 1998, doi: 10.1016/S0924-4247(98)00049-1.

[30] X. Zhang *et al.*, "Low-cost IMU Calibration with Nonlinear Scale Factors," *IEEE Trans Industr Inform*, vol. PP, p. 1, May 2021, doi:10.1109/tii.2021.3077296.

[31] A. El Fatimi, A. Addaim, and Z. Guennoun, "Software calibration for AK8963 magnetometer based on optimal ellipsoidal fitting," *International Journal of Electrical and Computer Engineering (IJECE)*, vol. 13, p. 2743, Jun. 2023, doi:10.11591/ijece.v13i3.pp2743-2751.

[32] A. Singh and D. Edla, "Auto-GeRo: An IOT based Geo Spatial Model for Real-Time Road Condition Detection," *SN Comput Sci*, vol. 5, Oct. 2024, doi: 10.1007/s42979-024-03362-7.

[33] A. Nugraha, D. Pambudi, A. Utomo, and D. Priyambodo, "Battery Charger Design in a Renewable Energy Portable Power Plant Based on Arduino Uno R3," 2022, pp. 147–161. doi: 10.1007/978-981-19-1804-9_12.

[34] J. Wang and N. Liu, "MEMS-IMU automatic calibration system design and implementation," *J Phys Conf Ser*, vol. 2492, p. 012005, May 2023, doi: 10.1088/1742-6596/2492/1/012005.